

# 1 **Impact Vaporization as a Possible Source of Mercury's Calcium Exosphere**

2  
3 Rosemary M. Killen, NASA Goddard Space Flight Center, Greenbelt, Maryland, USA  
4 Joseph M. Hahn, Space Science Institute, c/o Center for Space Research, University of Texas at  
5 Austin, 3925 West Braker Lane, Suite 200, Austin, TX 78759-5378, USA;  
6 [jhahn@spacescience.org](mailto:jhahn@spacescience.org)

7  
8  
9 Corresponding Author: R.M. Killen, Code 695, NASA Goddard Space Flight Center, Greenbelt,  
10 Maryland, 20771, USA. (rosemary.killen@nasa.gov); 301-286-6574

## 11 12 **Highlights**

- 13
- 14 • We show that Mercury's calcium exosphere, which is observed to vary seasonally about  
15 that planet's orbit, can be attributed to impact vaporization by interplanetary dust.
  - 16 • A comparison of models to MESSENGER observations shows that the seasonal  
17 variations in that Ca signal result from the planet's sizable orbital eccentricity and  
18 inclination which cause that planet to experience significant radial and vertical excursions  
19 through the interplanetary dust cloud.
  - 20 • The model developed here also requires an additional source localized at  $25 \pm 5^\circ$  degrees  
21 after Mercury's perihelion, and that may be due to a meteor stream possibly associated  
22 with the nearby comet Encke.
  - 23 • Impact vaporization can explain the source rate and true anomaly angle variations in the  
24 calcium exosphere but an additional mechanism must be invoked to explain the extreme  
25 temperature.
- 26  
27

27

28 **Abstract**

29

30 Mercury's calcium exosphere varies in a periodic way with that planet's true anomaly. We show  
31 that this pattern can be explained by impact vaporization from interplanetary dust with variations  
32 being due to Mercury's radial and vertical excursions through an interplanetary dust disk having  
33 an inclination within 5 degrees of the plane of Mercury's orbit. Both a highly inclined dust disk  
34 and a two-disk model (where the two disks have a mutual inclination) fail to reproduce the  
35 observed variation in calcium exospheric abundance with Mercury true anomaly angle.  
36 However, an additional source of impacting dust beyond the nominal dust disk is required near  
37 Mercury's true anomaly ( $\nu$ )  $25^\circ \pm 5^\circ$ . This is close to but not coincident with Mercury's true  
38 anomaly ( $\nu=45^\circ$ ) when it crosses comet 2P/Encke's present day orbital plane. Interestingly, the  
39 Taurid meteor storms at Earth, which are also due to Comet Encke, are observed to occur when  
40 Earth's true anomaly is  $\pm 20$  or so degrees before and after the position where Earth and Encke  
41 orbital planes cross. The lack of exact correspondence with the present day orbit of Encke may  
42 indicate the width of the potential stream along Mercury's orbit or a previous cometary orbit. The  
43 extreme energy of the escaping calcium, estimated to have a temperature  $>50000$  K if the source  
44 is thermal, cannot be due to the impact process itself but must be imparted by an additional  
45 mechanism such as dissociation of a calcium-bearing molecule or ionization followed by  
46 recombination.

47

48 **Keywords:**

49 Mercury, Atmosphere

50 Interplanetary Dust

51 Impact processes

52

53 **1. Introduction**

54

55 Mercury is surrounded by a surface-bounded exosphere with seven known components: H, He,  
56 O, Na, K, Ca and Mg. Calcium has been observed in Mercury's exosphere for over a decade,  
57 having been discovered by Bida et al. (2000) using the Keck telescope on Mauna Kea. The  
58 Mercury Atmospheric and Surface Composition Spectrometer (MASCS) instrument, a UV-  
59 visible spectrometer on the MErcury Surface, Space ENvironment, GEOchemistry, and  
60 Ranging (MESSENGER) spacecraft (McClintock and Lankton, 2007) has been taking  
61 spectroscopic measurements of neutral atoms and one ion ( $\text{Ca}^+$ ) in Mercury's exosphere  
62 since the first flyby of MESSENGER with Mercury in January, 2008. Limb scan observations

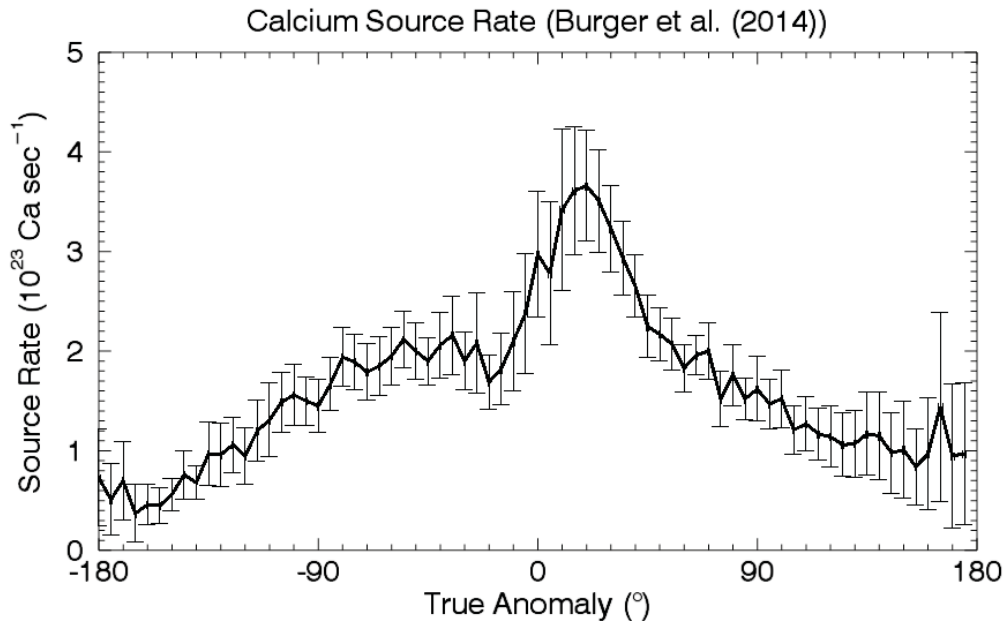
63 of the Ca exosphere of Mercury were analyzed in Burger et al., 2012 and 2014. They show a  
64 repeatable seasonal pattern in total source rate with respect to Mercury true anomaly angle,  $\nu$   
65 (Burger et al., 2014). (The true anomaly is the planet's angular coordinate measured from the  
66 direction of perihelion in the orbital plane.) In this paper we attempt to model the seasonal  
67 variations in the impact vaporization rate of calcium from Mercury's surface due to the influx of  
68 interplanetary dust. To explain a persistent enhancement at true anomaly angle  $25^\circ \pm 5^\circ$ , we also  
69 consider impact vaporization due to a meteor stream, possibly resulting from comet Encke whose  
70 orbit lies quite close to Mercury.

71  
72 In the following sections we first present the Ca observations obtained by MESSENGER's  
73 MASCS ultraviolet spectrometer (Section 2), then in Section 3 we discuss the models of the  
74 interplanetary dust disk that we will use (3.1), and finally we discuss our impact vaporization  
75 model (Section 3.2). In section 4 we discuss the results. The effect of varying the inclination of  
76 the dust disk is discussed in 4.1, and then we introduce the effect of a possible meteor shower in  
77 4.2. The discussion follows in Section 5; we briefly compare our results with previous work in  
78 section 5.1; then we discuss possible modes of energization of the neutral calcium in section 5.2,  
79 and finally in section 5.3 we discuss the fraction of impact vapor escaping at extreme  
80 temperature. Section 6 contains conclusions.

## 81 82 **2. Observations**

83  
84 Observations from the MESSENGER MASCS spectrometer show that the calcium exosphere  
85 is concentrated on the dawn hemisphere with a very wide distribution in local time. Data  
86 obtained by the MESSENGER MASCS spectrometer during more than 8 Mercury years  
87 (March 18, 2011 - March 17, 2013) were analyzed and published by Burger et al. (2014).  
88 Figure 1, derived from MESSENGER MASCS observations by Burger et al. (2014), shows the  
89 total source rate of Ca atoms into the exosphere over the whole planet in atoms  $s^{-1}$  derived  
90 from fits of MASCS data to the output of a Monte Carlo exosphere code. The source rate is  
91 remarkably repeatable over the orbital period of Mercury. The most intriguing part of this  
92 figure is the peak at true anomaly  $\nu=25^\circ \pm 5^\circ$ ; one might expect the peak to occur at  
93 perihelion,  $\nu=0^\circ$ , because interplanetary dust is concentrated sunward.

94



95  
 96 Figure 1. The total planetary calcium source rate into Mercury's exosphere is a periodic  
 97 function of Mercury true anomaly,  $\nu$ . Mercury is at perihelion when the true anomaly is  $0^\circ$   
 98 and at aphelion when the true anomaly is  $\pm 180^\circ$ . The black curve is the total calcium  
 99 source rate summed over the planet at each true anomaly angle, derived from observations  
 100 obtained by the MESSENGER MASCS spectrometer March 2011 - March 2013 (plot adapted  
 101 from Burger et al., 2014).

102  
 103 In addition to a true anomaly angle variation there is a marked dawn/dusk asymmetry in the  
 104 calcium exosphere (Burger et al., 2014). We know that the flux of large meteoroids at Earth has  
 105 been shown to be asymmetric with respect to the morning and evening hemispheres and to  
 106 depend on the position of the planet along its orbit and on the particle size (e.g. Fentzke and  
 107 Janches, 2008; Janches et al., 2006), and we expect the same to be true at Mercury. The ratio of  
 108 impacts on morning to evening on Mercury's surface was derived by Marchi et al. (2005) to be  
 109 about 1.2 - 1.5 at perihelion and about 0.8 - 1 at aphelion. Given that the column abundance of  
 110 Ca,  $N$ , is on the order of  $1 \times 10^9 \text{ cm}^{-2}$ , and the derived e-folding distance,  $H$ , is about  $4 \times 10^8 \text{ cm}$ ,  
 111 the maximum number density of Ca at the morning terminator,  $N/H$ , is only about  $3 \text{ cm}^{-3}$ , and a  
 112  $3/2$  asymmetry would imply a density at the evening terminator of  $< 2 \text{ cm}^{-3}$ . The MASCS  
 113 sensitivity is such that a column density of  $< 1.5 \times 10^8$  would be undetectable. The Burger (2014)  
 114 model does a good job of fitting the observed spatial pattern in the exospheric abundance with a  
 115 dawn source because of redistribution of vapor in the exosphere.

116

117 The following section provides an explanation for the seasonal variation in the abundance of  
118 Mercury's exospheric Ca. In subsequent sections we address other observations that are not yet  
119 completely understood, including the Ca component's extreme temperature.

120

### 121 **3. Models**

#### 122 **3.1 Model of the dust disk**

123

124 We seek to determine whether the observed variation with true anomaly angle,  $\nu$ , observed  
125 in Mercury's Ca exosphere can be explained by impact vaporization by interplanetary dust.  
126 To that end we have modeled the impact vaporization rate at Mercury as a function of  
127 Mercury's position in the interplanetary dust cloud.

128

129 The cloud of interplanetary dust in the inner heliosphere is disk-like, with its dust  
130 concentrated in a plane that lies near the ecliptic. To model the dust flux onto Mercury, we  
131 employed a dust-disk model derived by Hahn et al. (2002), fitted to optical observations of  
132 dust whose heliocentric orbits are also in the vicinity of Mercury and Venus. In brief, this  
133 model assumes three dust sources, denoted by subscript  $j$ : 1) asteroids and Jupiter-family  
134 comets, 2) Halley type comets, and 3) Oort cloud comets and interstellar sources,  
135 respectively.

136

137 The spatial distribution of interplanetary dust is written as the sum over several  
138 components, one being an isotropic source from the Oort cloud comets, and the other two  
139 having inclination distributions that are Gaussian. The inclination distributions are taken  
140 from Hahn et al., 2002, section 4.2.1, which can be consulted for further details. Each source  
141 has a unique inclination distribution  $g_j(i)$  with respect to the dust disk midplane:

142

$$g_j(i) = \frac{2}{\pi} \sin(i) \times \begin{cases} 1, & j=\text{iso} \\ c_j e^{-(i/\sigma_j)^2/2}, & \text{otherwise} \end{cases} \quad (1)$$

143

144 where  $g_j(i)$  is the fractional abundance of population  $j$ 's dust that has inclination  $i$ . Each source  
145 population  $j$  produces dust that has a latitude distribution,  $h_j(\beta)$ , that is:

146

147

$$h_j(\beta) = \int_{\beta}^{\pi/2} \frac{g_j(i) di}{\sqrt{\sin^2 i - \sin^2 \beta}} \quad (2)$$

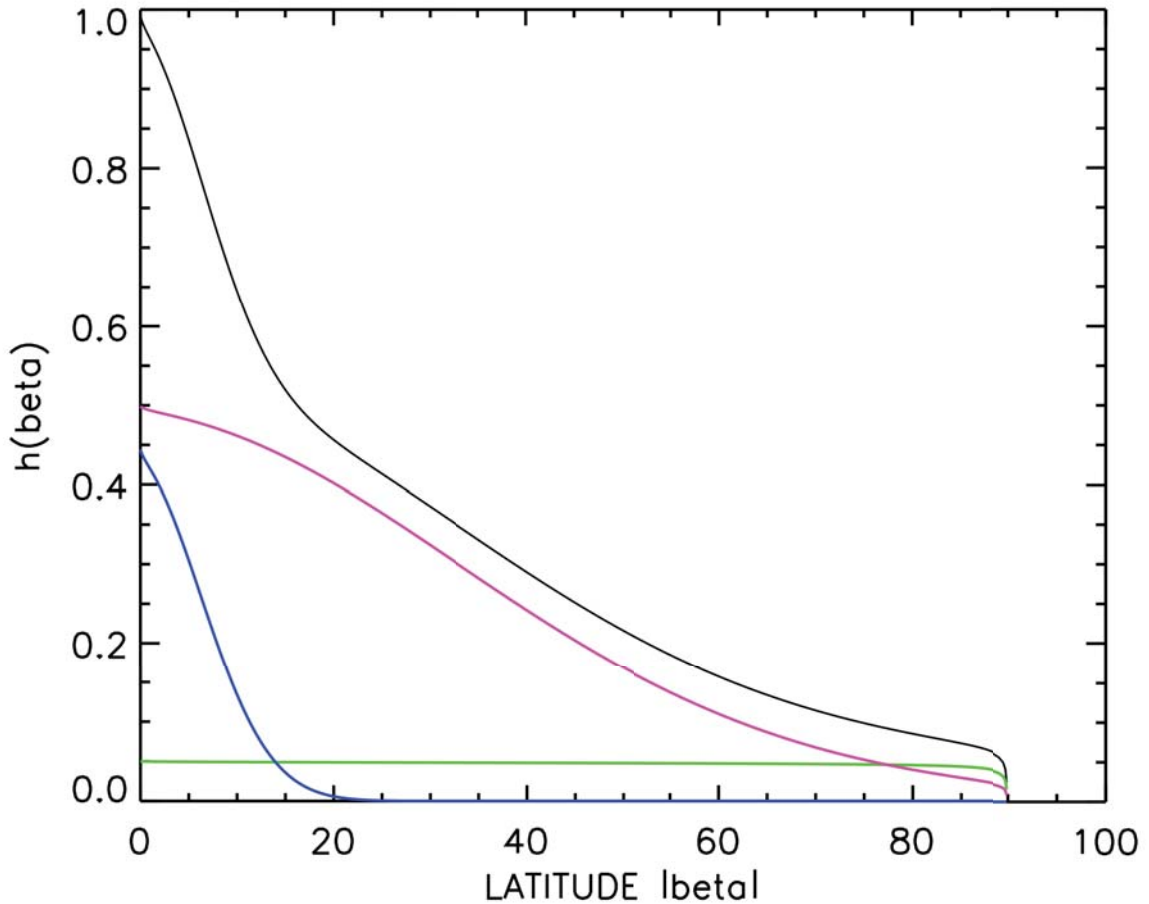
148

149 In other words, each dust particle is in orbit with a particular inclination,  $i$ , with respect to  
 150 the dust disk's mid-plane, and these inclinations are integrated to obtain the dust density at  
 151 a particular latitude,  $\beta$ . Here the dust density is assumed to vary as

$$n(R, \beta) \propto R^{-\chi_j} h_j(\beta) , \quad (3)$$

153 where  $R$  is the polar radial coordinate from the Sun, so this factor accounts for radial  
 154 changes in dust density of population  $j$ 's dust at latitude  $\beta$  above/below the dust disk's  
 155 midplane, which itself is likely to be tipped no more than a few degrees from the ecliptic  
 156 plane (Figs 5 and 12 of Hahn et al., 2002).

157



158

159

160 Figure 2.  $h(\beta)$  (black curve) is the abundance of dust at latitude  $\beta$  relative to that in the  
 161 dust-disk's midplane at  $\beta=0$  (Hahn et al., 2002), with  $\beta$  related to the cylindrical  
 162 coordinates  $R, z$ , via  $\tan(\beta)=z/R$ . The three populations of interplanetary dust are: lower  
 163 inclination dust generated by colliding asteroids and outgassing Jupiter family comets  
 164 (blue), higher inclination dust generated by Halley type comets (magenta), and isotropic  
 165 dust produced by Oort cloud comets (green).

166  
 167 Each population's density varies in heliocentric distance with a distinct power law  $\propto R^{-\chi_j}$ .  
 168 The three populations are: dust from asteroids and Jupiter family comets having  
 169 characteristic inclinations  $\sigma_j=7^\circ$  (low); dust from Halley-type comets with typical  
 170 inclinations  $\sigma_j=33^\circ$  (extended); and an isotropic source from Oort cloud comets whose  
 171 inclination distributions are uniform thus  $g_j=1$  in Equation 2. The populations are also  
 172 weighted by a factor  $f_j$  that provides the relative weight of the dust population  $j$  and  $\chi$  is the  
 173 radial dependence of that population (see Table 1).

174  
 175 Table 1. Nominal parameters of the 3 populations of interplanetary dust.

Population	$f_j$	$\chi_j$
low	0.45	1.00
high	0.50	1.45
isotropic	0.05	2.00

176  
 177 The vaporization of dust that is impacting Mercury will depend on the dust density and its  
 178 relative speed, both of which vary with that planet's true anomaly  $v$ . The relative orientations of  
 179 the dust disk to the orbit of Mercury will affect the dust flux to the surface, so these results will  
 180 be sensitive to the inclination of the dust-disk relative to Mercury's orbital plane, as well as to the  
 181 dust disk's longitude of the ascending node  $\Omega$ , which in this study will be measured in  
 182 Mercury's orbital plane from Mercury's longitude of perihelion (i.e. when Mercury is at  $v=0$  in  
 183 Figure 1).

184  
 185 The most uncertain elements of the dust disk model are the tilt of the dust disk's midplane  
 186 relative to Mercury's orbital plane and the orientation of the disk's midplane. That tilt and  
 187 orientation of the dust disk can be described by an inclination,  $i$ , that is probably no more than a  
 188 few degrees from the ecliptic (see Figs 5 and 12 of Hahn et al., 2002), and by the longitude of the  
 189 ascending node,  $\Omega$ , which is the ecliptic longitude where the dust-disk's mid-plane crosses the  
 190 ecliptic plane. Estimates of  $\Omega$  range from  $\Omega=87^\circ\pm 4$  (Leinert et al., 1980; Helios data);  $77.7^\circ\pm 0.6$   
 191 (DIRBE model);  $66^\circ$  (Leinert et al., 1976), to  $53^\circ$  (Reach, 1991). In our models, in order to

192 determine the best fit to the seasonal variation in the Ca source rate, we varied the inclination of  
193 the dust disk, the dust disk's longitude of ascending node, and also the radial power,  $\chi$ , of the low  
194 population dust.

195

### 196 **3.2. Impact Vaporization Model**

197

198 We have used the impact vaporization model previously described in Morgan and Killen (1998)  
199 and in Killen et al. (2005). This model is based on the planar impact approximation (Melosh,  
200 1989) with parameters from Melosh (1989) and Lange and Ahrens (1982). The equations are  
201 given in Killen et al. (2005) Appendix I. The density of the impacting interplanetary dust was  
202 computed using the Hahn et al. (2002) model, with dust impact velocity drawn from the velocity  
203 distribution of Cintala (1992), equation (A11a). The dust-density variation with heliocentric  
204 distance is already included in the Hahn formalism, so we used Cintala's Eqn (A11a) rather than  
205 (A11b). Gravitational focusing is accounted for in the Cintala (1992) formalism. The dust impact  
206 model used here accounts for variation in the impacting dust flux that is due to Mercury's radial  
207 and vertical motion through the interplanetary cloud that are a result of Mercury's substantial  
208 eccentricity and inclinations. The dust flux at Mercury is scaled from that at Earth using equation  
209 A11a of Cintala (1992) assuming the Love and Brownlee (1993) accretion rate of cosmic dust at  
210 the Earth is  $4\pm 2 \times 10^7$  kg/yr. Our formalism accounts for gravitational focusing by Mercury.

211

212 The vaporization rate is calculated as a function of the impacting dust velocity and is integrated  
213 over the velocity function (Killen et al., 2005; Appendix I), which has a median impact speed of  
214 20 km/s at Mercury (Cintala, 1992). According to Collette et al. (2014) the impact vaporization  
215 as a percent of projectile mass is about 40% at an impact velocity of 20 km/s (the highest impact  
216 velocities they reported), which is consistent with the O'Keefe and Ahrens (1977) condition that  
217 we use, namely that significant vaporization commences at  $v_i/v_{\text{sound}}=3.1$ , where  $v_i$  is the impact  
218 velocity and  $v_{\text{sound}}$  is the velocity of sound in the target. The velocity of sound in rock forming  
219 silicate materials is 5 - 8 km/s, so the onset of significant vaporization is 16 - 25 km/s. Our  
220 impact vaporization rate  $f_v(v_i)$  is scaled to

$$221 \quad f_v(v_i) = \frac{\rho_m}{\rho_t} \left\{ \frac{v_i}{v_{\text{sound}}} \right\}^2, \quad (4)$$

222

223 where  $\rho_m$  is the density of the meteoroid,  $\rho_t$  is the density of the target. Additional model  
224 parameters are reported in Table 3 and the meaning of quantities such as  $c_{\text{type}}$ ,  $m_{\text{type}}$ , and  $i_{\text{type}}$   
225 are detailed in Killen et al. (2005). Basically they are set to choose the type of impactor and  
226 target. In particular, the target material here is assumed to be regolith whose thermodynamic



227 constants are from Cintala (1992). The projectile dust grain is assumed to be a carbonate  
228 meteoroid and the constant C in Table 3 is related to the bulk speed of sound while  
229 dimensionless constant S is obtained from shock-wave experiments. That quantity enters into the  
230 linear shock-particle velocity equation of state. Because we do not have all physical quantities  
231 for "regolith" other target quantities (having subscript t) assume the target is basalt while the  
232 projectile quantities (subscript p) assume calcite (see Melosh, 1989, page 232).

233  
234 Given that more than half of the micrometeoritic flux is impacting Mercury at velocities greater  
235 than 20 km/s (Cintala 1992), significant vaporization is expected. In fact, our result may be an  
236 underestimate because the velocity distribution at Mercury calculated by Marchi et al. (2005)  
237 was double-peaked, with a second peak at about 40 km/s. Marchi et al. (2005) report a mean  
238 impact velocity for all of their distributions of about  $30 \text{ km s}^{-1}$ , but with double peaks (one at 30  
239 km/s and one at 40 km/s) and with tails spanning from about 15 to  $80 \text{ km s}^{-1}$ . Thus the Marchi et  
240 al. (2005) velocity distribution at Mercury is shifted to higher impact velocities by about 20 km/s  
241 from the one we use. However, their velocity distribution only applies to meteoroids coming  
242 from the Main Belt, and not dust in general. We tested the effect of increasing the mean impact  
243 velocity to 35 km/s, but because mass density and velocity both affect the flux, in our model the  
244 higher velocity stream simply requires a lower dust density. We cannot simultaneously constrain  
245 dust density and velocity without a constraint on one or the other. The velocity distribution  
246 derived by Borin et al. (2009) for small particles (radius of  $5 \mu\text{m}$  and  $100 \mu\text{m}$ ) has a slightly  
247 lower mean velocity than that of Cintala (1992) and a much less extended high velocity tail. We  
248 conclude that the Cintala distribution (in between the Borin et al. and the Marchi et al. results) is  
249 probably reasonable for small particles, which make up the more or less constant background, as  
250 opposed to large meteors that are sporadic and widely distributed in frequency. The highly  
251 repeatable seasonal pattern in the exosphere cannot be attributed to sporadic meteors.

252  
253 Although the porosity of Mercury's regolith is high, we have assumed zero porosity in these  
254 calculations because our code does not compensate for sticking of atoms to regolith grains on  
255 multiple encounters with soil. Higher porosity will increase the derived vaporization rate by up  
256 to a factor of  $\sim 5$ . However, only about one third of this will escape the regolith due to  
257 interactions with the soil (Cassidy and Johnson, 2005). The assumption of zero porosity  
258 compensates for lack of a more detailed treatment of multiple scattering, and it gives a  
259 conservative estimate of vapor that escapes into the exosphere. Another, possibly greater, source  
260 of uncertainty is the amount of impact vapor that remains in the uncondensed state after the  
261 initial fireball becomes collisionless (e.g. Berezhnoy and Klumov, 2008). Our code gives the  
262 total vapor phase (as opposed to melt plus vapor) and we assume that the calcium is released in

263 the molecular state. We assumed 3.5% ( $\pm 0.7$ )% Ca in the regolith by number (Evans et al.,  
 264 2012). Both the regolith and impacting dust contribute to the vapor. We assume that the  
 265 impacting dust and the regolith have the same Ca fraction. Because this is a global average  
 266 calculation, we have not considered spatial variations in the Ca abundance in the Mercury soil.  
 267 However, we note that a spatially asymmetric Ca abundance in the soil would produce a bi-  
 268 annual variation due to the spin-orbit coupling of the planet's motion, not the annual variation  
 269 that is seen. The low abundance of Ca in the lunar and Mercurian exospheres is explained by the  
 270 condensation of Ca into dust grains during expansion of the cooling impact-produced vapor  
 271 cloud (Berezhnoy, 2010).

272  
 273 The fraction of uncondensed atomic Ca that is observed at high altitude by the MASCS  
 274 instrument is a free parameter in our model and is scaled to match the data: it is generally less  
 275 than 10% as discussed in section 4. This fraction varies slightly for different assumptions, and is  
 276 most sensitive to the radial dependence of the dust density, which we varied. The remaining  
 277 thermodynamic constants used in the impact vapor code are also given in Table 3.

278  
 279 Table 3. Thermodynamic Constants and Surface/Projectile Constants used

parameter	value	Comments
$\rho_{\text{target}}$ (Kg/m <sup>3</sup> )	1800	
$\rho_{\text{impactor}}$	1800	
fraction Ca	0.0354	
porosity	0.0	Gives a lower limit on impact vaporization rate
$v_{\text{esc}}$ (km/s)	4.25	Mercury escape velocity
mass number (AMU)	40	
radius target (km)	2340	
c <sub>type</sub>	3	H <sub>v</sub> =9.64E10; regolith
m <sub>type</sub>	1	used to calculate the minimum velocity for vaporization; Al onto enstatite; aa=21.014, bb=-14.154, cc=3.058 $v_{\text{min1}}=(aa+bb*m+cc*m^2)$ ; m=distention
i <sub>type</sub>	1	siliceous impactor
C <sub>t</sub> (km/s)	2.60	basalt target; Melosh, 1989; Table AII.2; Linear shock-particle velocity equation of state parameters; related to the bulk sound speed
S <sub>t</sub>	1.62	basalt target; related to the Gruneisen parameter $\Gamma$
C <sub>p</sub> (km/s)	3.80	carbonate projectile
S <sub>p</sub>	1.42	carbonate projectile

280  
 281  
 282 **4. Results**

283

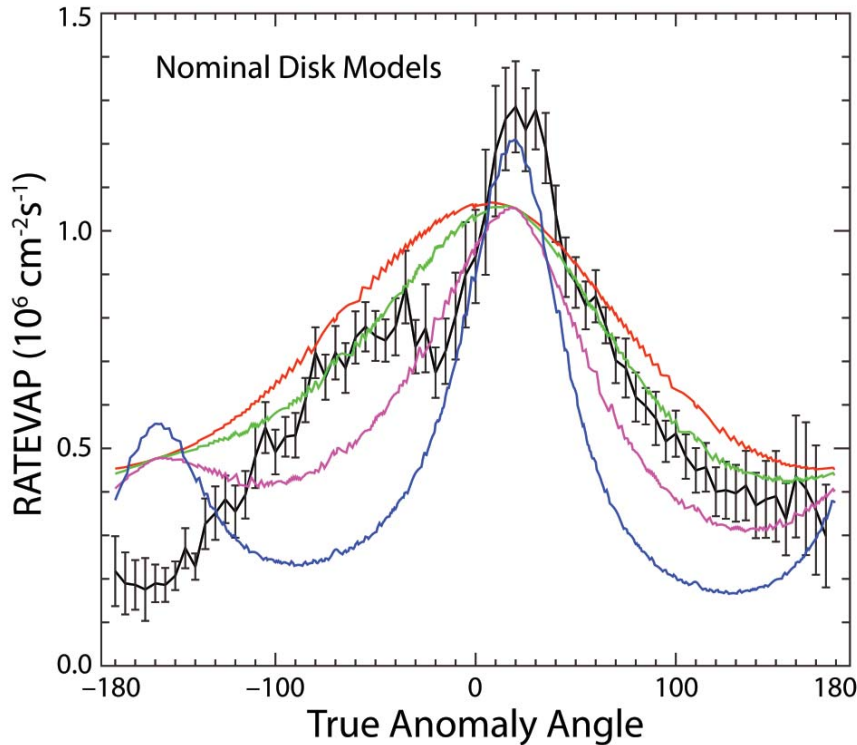
284 The following shows results from selected models that calculate the rate at which Mercury  
285 sweeps up interplanetary dust and produces Ca vapor via impacts. This rate varies  
286 seasonally due to Mercury's substantial radial and vertical motion through the circumsolar  
287 dust-disk. Section 4.1 will consider how the Ca production rate varies with the dust-disk's  
288 relative inclination, which controls how far Mercury travels from the dust-disk's midplane  
289 and thus alters the local dust density. Section 4.2 will show that an additional source of  
290 dust is needed to explain the Messenger observations, and it is suggested that the dust  
291 could be due to a meteor storm associated with the nearby comet Encke.

292

#### 293 **4.1 Effect of varying the inclination of a nominal dust disk**

294

295 In Figure 3 we show the effect of varying the inclination of the dust disk from  $45^\circ$  to a low  
296 inclination dust disk of  $5^\circ$ . The impact vaporization rates shown in Figure 3 as a function of true  
297 anomaly angle,  $\nu$ , vary as the planet traverses the modeled dust disk. The coordinate system used  
298 here and in Figures 4 and 7, is in the plane of Mercury's orbit so the dust disk's inclination,  $i$ , is  
299 measured relative to Mercury's orbital plane. This coordinate system's  $x$  axis is oriented towards  
300 Mercury's perihelion, and all longitudes will be measured from the  $x$  axis. Consequently the dust  
301 disk's longitude of ascending node,  $\Omega$ , will also be Mercury's true anomaly,  $\nu$ , when it passes  
302 through the dust-disk's midplane, which happens again at  $\nu = \Omega \pm 180^\circ$ . For a low inclination disk,  
303 the maximum impact vaporization rate occurs at Mercury's perihelion because in this case the  
304 heliocentric radial excursion dominates the impactor flux variation. As the inclination increases,  
305 the maximum in source rate occurs where Mercury's orbital plane crosses the dust disk plane at  
306 the minimum heliocentric radial distance. But also note that a secondary peak occurs where the  
307 two planes cross again at the larger radial distance.



308

309 Figure 3. Ratevap is the rate at which atomic calcium is ejected into the exosphere. It is the  
 310 fraction of the impact vaporization rate of Ca-bearing minerals in all forms, including molecular,  
 311 that remains in the uncondensed state at the point when the vapor cloud becomes collisionless.  
 312 We have plotted ratevap vs.  $\nu$  for a dust disk with ascending node  $20^\circ$ . The figure shows how  
 313 results are sensitive to the dust disk's inclination,  $i$ , and shows why a single disk model cannot  
 314 account for the observed seasonal variations in exospheric Ca. Only the inclination relative to  
 315 Mercury's orbital plane is different for each model:  $i=5$  (red),  $i=10$  (green),  $i=20$  (magenta) and  
 316  $i=45$  (blue) degrees, respectively. The fraction of Ca-bearing vapor that remains in the  
 317 uncondensed state is set at 12% for all of these runs for comparison purposes. The vaporization  
 318 rate is in units of  $10^6$  atoms  $\text{cm}^{-2} \text{s}^{-1}$ . The data are shown in black. None of these models can  
 319 fit the data (black). To keep the parameters constant except inclination, we have not attempted a  
 320 best-fit model here.

321

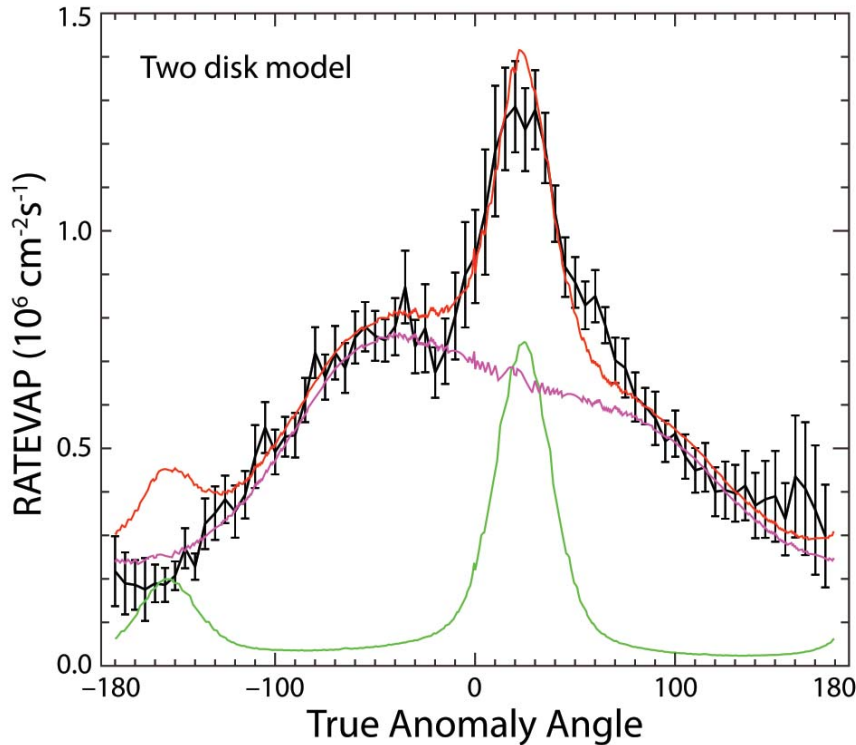
322 Although the increased Ca source rate at Mercury  $\nu=25^\circ \pm 5^\circ$  could in principle be caused by a  
 323 highly inclined dust disk (e.g. blue line in Figures 3), an increased vapor rate would also occur  
 324 near aphelion,  $\nu = -160^\circ$  where the two planes cross again. This is not seen in the data (black  
 325 curve). This secondary peak would be due to Mercury passing through the dust-disk's midplane  
 326 again but this time just after apoapse where the dust density is smaller than at periapse. Because  
 327 this secondary peak is not seen in the data, shown in black, the inclination of the dust disk with  
 328 respect to Mercury's orbital plane is constrained to be less than about  $10^\circ$  (green curve in Figure

329 3). But in this case there still remains an additional source that is unaccounted for. Observations  
330 of the zodiacal light show that the dust disk midplane is certainly no more than a few degrees  
331 away from the ecliptic plane (Hahn et al., 2002). Leinert et al. (1980) estimate that the dust-disk  
332 ecliptic inclination is  $i=3.3^\circ \pm 0.4^\circ$  with an ascending node  $\Omega=77^\circ \pm 10^\circ$  while Misconi and  
333 Weinberg (1978) report  $i=2.7^\circ$  with  $\Omega=85^\circ$ . Therefore the dust disk's mid-plane with respect to  
334 Mercury's orbital plane is probably between  $3^\circ$  and  $10^\circ$ . The final fraction of Ca-bearing vapor in  
335 the uncondensed atomic state is set at 12% of the total Ca-bearing vapor emitted in each of the  
336 simulations in Figure 3, chosen to most closely fit the observations. Note that a secondary peak  
337 in the simulations of Ca signal near  $\nu=-160^\circ$  (Fig. 3) could be avoided if the dust density falls off  
338 much more rapidly with heliocentric distance,  $R$ . However, a steep radial gradient in the dust  
339 disk is contrary to dust models based on the zodiacal light (e.g., Hahn et al., 2002), and can be  
340 rejected.

341  
342 In Figure 4 we show a nominal low inclination disk (magenta) with a radial dependence  $r^{-2}$ , and a  
343 high inclination disk (green) with a radial dependence  $r^{-3}$ . Although the steep radial dependence  
344 of dust density minimizes the secondary impact vaporization peak, it does not eliminate the  
345 secondary peak at  $\nu=-150^\circ$ . Because this high inclination model (green) is calibrated to  
346 measurements at 1 AU, the fraction of total vapor that is seen in the uncondensed state for the  $r^{-3}$   
347 model is only 0.02 (2%), much less than the fraction in Figure 3. The actual amount of vapor  
348 remaining in the atomic uncondensed state after the initial fireball becomes collisionless will be  
349 similar because it must be scaled to match the data.

350  
351 So to summarize, none of the nominal dust disk models considered thus far provide an adequate  
352 fit to the data.

353  
354



355  
356

357 Figure 4. The impact vaporization rate of Ca vs.  $\nu$  for two dust disks at a high relative  
358 inclination. The rate is in units of  $10^6$  atoms  $\text{cm}^{-2} \text{s}^{-1}$ . Dust disk 1 (magenta) has inclination  $10^\circ$   
359 with respect to Mercury's orbital plane, ascending node  $290^\circ$ , radial dependence  $R^{-2}$ ; dust disk 2  
360 (green) has inclination  $45^\circ$ , ascending node  $25^\circ$ , and radial dependence  $R^{-3}$ , with the sum of the  
361 two disks plotted in red, and the data in black. We reject the steep radial dependence model.

362

#### 363 4.2 Effect of a Meteor Stream

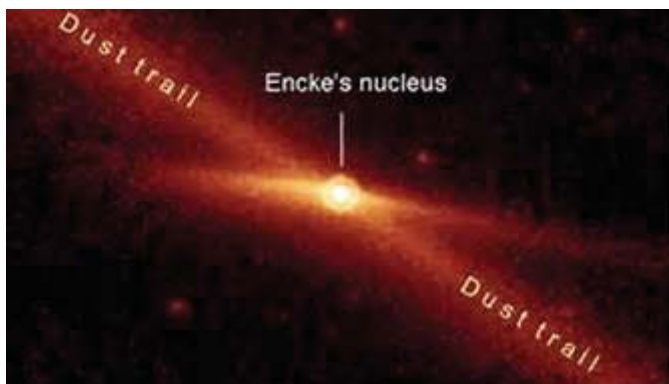
364

365 The enhancement in Ca source rate near true anomaly angle  $25^\circ \pm 5^\circ$  cannot be modeled by  
366 impact vaporization from a single dust disk (Figure 3) because such a disk would cause two  
367 enhancements in the vapor rate, one at each node where the two planes cross (once when  
368 Mercury's true anomaly equals the disk ascending node and then again when Mercury's  
369 true anomaly equals the disk ascending node plus  $180^\circ$ . For a similar reason we cannot find  
370 a satisfactory fit using an interplanetary dust model that is composed of two circumsolar  
371 dust disks (Figure 4). So for these reasons we now consider whether the observed Ca  
372 excess at  $\nu = 25^\circ \pm 5^\circ$  could be due to a meteor storm, which is a concentration of dust that  
373 is localized at or near a comet's orbit about the Sun. And in the following we focus on  
374 possible meteor storms from comet Encke, which is a short period comet that has produced

375 a dust trail all along its orbit (see Figure 5), and whose orbit comes very close to Mercury's  
376 orbit.

377  
378 Although dust ejected from a comet is subject to additional forces, (radiation pressure, Poynting-  
379 Robertson (PR) drag, and gravitational perturbations due to the planets) cometary dust grains  
380 will nonetheless tend to remain concentrated in the vicinity of the comet's orbital plane. Dust  
381 from Encke will drift radially through its orbit plane due to solar Poynting-Robertson drag  
382 (Burns et al., 1979). Encke meteor showers might be expected at Mercury true anomaly  $\nu=46^\circ$   
383 because this is the longitude where the two planes cross and the orbits are in close proximity  
384 (Fig. 6). Encke and the Taurids are believed to be remnants of a much larger comet, which  
385 disintegrated over the past 20000 to 30000 years (Whipple, 1940; Klacka, 1999). Planetary  
386 gravitational perturbations will drive additional orbital evolution both of the comet and its dust,  
387 and that evolution is not strictly coplanar. In particular, planetary perturbations can drive the  
388 comet dust out of the comet's orbital plane, which would then allow Mercury to encounter that  
389 dust over a broader range of true anomalies. At Earth, Encke contributes several meteor showers  
390 that occur at various longitudes that differ by  $\sim 20^\circ$ , including the Taurid meteor showers whose  
391 temporal span is 20 - 25 days or about 20 degrees of longitude at Earth. Consequently a shower  
392 of Encke dust at Mercury could conceivably occur at  $\sim 20$  degrees before Mercury has passed  
393 through Encke's orbit plane which would then account for the excess exospheric Ca observed at  
394  $\nu=25^\circ \pm 5^\circ$  in Fig. 1.

395  
396



397  
398 Figure 5. An infrared image from Spitzer Space Telescope obtained 22 July, 2004, shows Comet  
399 Encke's nucleus and dust trail (Courtesy NASA/JPL-Caltech and M. Kelley, Univ. of  
400 Minnesota).

401  
402 The orbital parameters of comet 2P/Encke (epoch 2013) are given in Table 2.

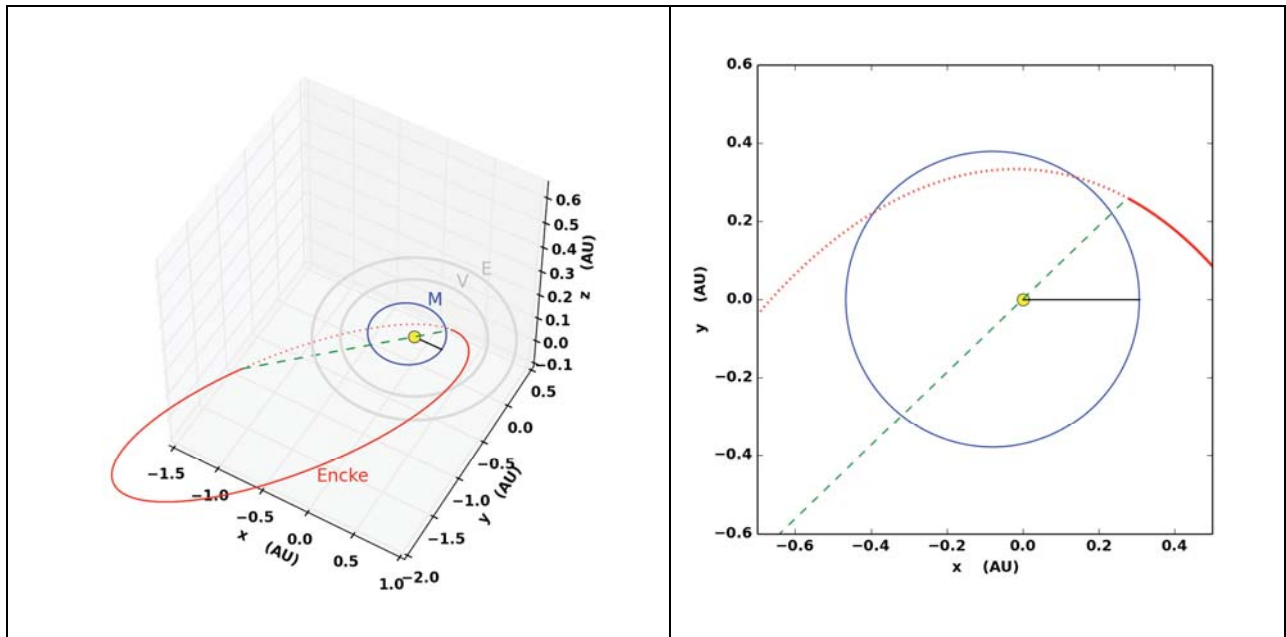
403



404 Table 2. Orbital Elements for Comet 2P/Encke

Orbital Elements of Comet 2P/Encke (J2000)	
Longitude of Perihelion (deg)	186.53563
Longitude of Ascending Node (deg)	334.57
Inclination (degrees)	11.77897
Eccentricity	0.8482322
Semi-major axis (AU)	2.2147
Period (years)	3.30
Periapse distance (AU)	0.3361267

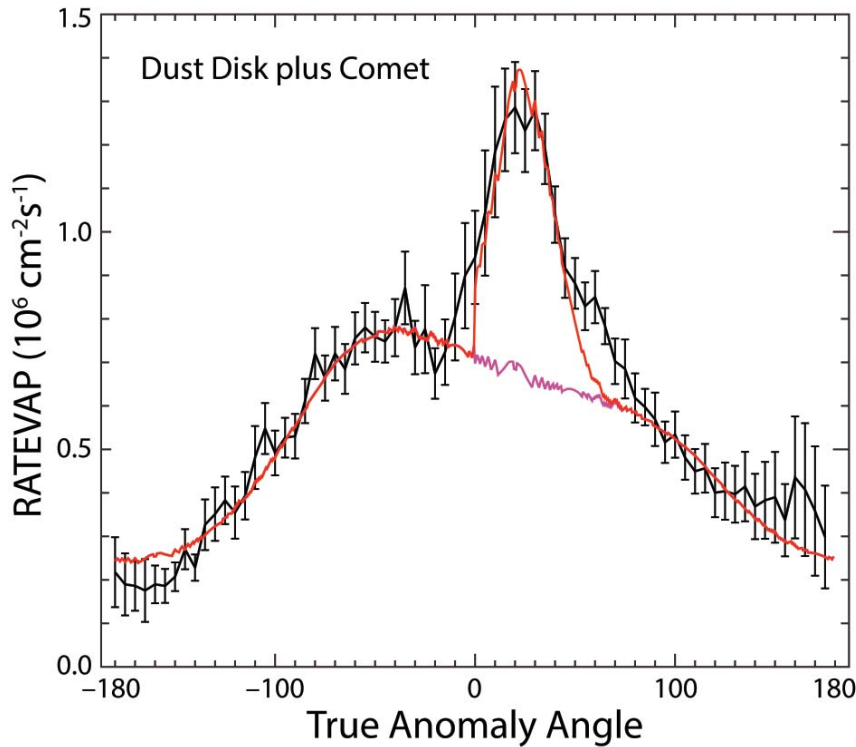
405  
406  
407  
408  
409



410  
411 Figure 6. (left) Encke's orbit (red) is shown along with those of Mercury (blue), Venus and Earth  
412 (in grey). The coordinate system used here has its x-y plane in Mercury's orbit plane, the  
413 direction of the +x axis is towards Mercury's periastron, and the angles described below are  
414 measured counter clockwise from this x-axis. In this coordinate system, Encke's longitude of  
415 ascending node is  $226^\circ$  and its descending node is at  $46^\circ$ , and these angles are also Mercury's  
416 true anomaly when it crosses Encke's orbit plane. The dashed green line is where these two orbit  
417 planes cross. Encke's orbit (red) is projected onto Mercury's orbital plane (the x-y plane) in the  
418 right panel. The black line is drawn from the sun (yellow circle) to Mercury's periastron.



419  
420  
421



422  
423 Figure 7. Ca vaporization rate at Mercury due to the interplanetary dust-disk (magenta  
424 line) plus a cometary stream whose peak density occurs at true anomaly  $\nu=25^\circ$ . The  
425 Gaussian half-width of the cometary dust stream extends  $\pm 15^\circ$  when measured in units of  
426 Mercury's true anomaly, and the rate is in units of  $10^6 \text{ atoms cm}^{-2} \text{ s}^{-1}$ . The red line is the  
427 summed contributions from the cometary dust stream plus that due to an interplanetary  
428 dust-disk that is inclined  $10^\circ$  from Mercury's orbital plane, and whose ascending node is  
429  $290^\circ$  when measured from Mercury's longitude of perihelion, with the dust density varying  
430 as  $R^{-2}$ , where  $R$  is the heliocentric distance. The MASCS observations are plotted in black. In  
431 this model the fraction of Ca-bearing vapor that remains in the uncondensed state when  
432 the vapor cloud becomes collisionless is 5.5%.

433  
434 Figure 7 shows how Mercury's exospheric Ca signal varies with the planet's true anomaly  $\nu$   
435 when the impacting dust is the sum of two sources: a single circumsolar dust-disk plus that due  
436 to a cometary dust stream whose centroid lies at Mercury true anomaly,  $\nu$ ,  $25^\circ$ . Note that  
437 MESSENGER MASCS observations constrain the a Gaussian half width of the model's  
438 cometary dust stream to about  $15^\circ$  of Mercury's orbital longitude whereas the full width at half-  
439 maximum (FWHM) of the Encke dust stream was previously estimated to be  $50^\circ$  at Mercury

440 (Selsis et al., 2004). Although Mercury passes through Encke's orbit plane twice, the second  
441 instance occurring when Mercury's  $\nu=226^\circ$ , no contribution from the second crossing is included  
442 in this model because Encke's and Mercury's orbits are now several astronomical units apart.  
443

444 To explore how results vary with dust velocity we also performed an additional simulation with  
445 impact speeds increased by 15 km/s. Although the higher impact velocity does increase the  
446 impact vaporization rate, increased velocity can be offset by reducing the number density of the  
447 impacting dust. Because the model's two principal parameters (dust density and dust impact  
448 speed) are coupled in this way, this study can only provide plausible estimates rather than firm  
449 measurement of both quantities. Nonetheless this uncertainty does not impact our main findings:  
450 that the seasonal variations in Mercury's exospheric Ca can be attributed to impacts by  
451 interplanetary dust grains plus an additional localized contribution that could be a meteor stream  
452 from the nearby comet Encke.  
453

454 Unlike the meteor streams due to comets Bradfield and Tempel-Tuttle, which impact Mercury at  
455 about 70 km/s and at high latitudes, the Encke dust grains impact Mercury with a mean velocity  
456 of about 28 km/s and at low latitudes (Christou and Asher, 2009). These velocities are only  
457 slightly higher than the mean velocity expected from the dust at Mercury, about 20 km/s  
458 (Cintala, 1992). Since all of the MASCS Ca observations analyzed by Burger are from equatorial  
459 limb scans, we cannot determine from these data whether there is an effect from those comets  
460 that impact at high latitudes.  
461

## 462 **5. Discussion**

### 463 **5.1 Comparison with earlier work**

464 Kameda et al. (2009) analyzed the possibility that variations in Mercury's sodium  
465 exosphere are the result of excursions of Mercury with respect to the interplanetary dust  
466 disk. They used data from Mercury's sodium exosphere to derive parameters for a dust  
467 distribution based on a least-squares fit to the  $\nu$  variation of Mercury's exospheric sodium.  
468 They assumed a dust density distribution with heliocentric distance,  $R$ , and distance from  
469 the symmetry plane of the dust-disk,  $z$  (assumed to be at an inclination of 2.9 degrees from  
470 the ecliptic) with the following functional form:  
471  
472  
473

$$n_{IPD} \propto R^{-\alpha} \exp[-\beta(\frac{z}{R})^2]$$

(5)

474

475

476 The parameters  $\alpha, \beta$  are free parameters in their model and are fit to the Mercury Na  
 477 exospheric observations. They also allowed the longitude of the ascending node,  $\Omega_d$ , and  
 478 inclination,  $i$ , of the dust disk to be free parameters, resulting in  $i > 1.9$ , and  $-104 < \Omega_d < 57$ .  
 479 Their derived fit is  $\beta = 50, \alpha = 0.2$ . The Kameda model is therefore a thin flat disk that  
 480 decreases very little with radial distance from the Sun, but decreases rapidly with latitude.

481

482 Our results are consistent with dust models derived from observations of the zodiacal light,  
 483 HELIOS data or the DIRBE model (Reach, 1991; Leinert et al., 1980; 1976), which conclude  
 484 that  $\alpha \sim 1.5 - 2$ . According to Reach (1991) the dust albedo varies as  $R^{-0.3}$ , not the density.

485

## 486 **5.2 Processes imparting additional energy to the atomic calcium**

487

488 Based on the line-widths and scale heights of the ground-based data, Killen et al. (2005)  
 489 derived a temperature of the atomic Ca in the range of 12000-20000 K, much higher than  
 490 the range of temperatures derived from other known species such as Na (1200 K). Killen et  
 491 al. (2005) suggested that the hot Ca seen in the exosphere is a result of a source consisting  
 492 of calcium-bearing molecules that are dissociated in the exosphere, thereby obtaining  
 493 excess energy in the process.

494

495 Recently, Burger et al. (2014) derived a temperature for the Ca exosphere in excess of  
 496 50000 K using MESSENGER MASCS data. His method was to run a Monte Carlo code with the

497 source's temperature, size, and rate as free parameters to minimize the  $\chi^2$  statistic between

498 various assumed source temperatures and do a least squares fit with the model output and

499 data. This method gave a most likely temperature of 70000 K. Mg, also seen in Mercury's

500 exosphere, is similar to Ca in that it has a component of extreme temperature with a source  
 501 concentrated on the dawn side, although it may also have a lower temperature component,

502 consistent with impact vaporization at 3000 K (Sarantos et al., 2011). Because sodium is a

503 much more volatile element, its source processes are dominated by photon-stimulated

504 desorption (Cassidy et al., 2014), with a characteristic temperature of 1200 K. Temperatures

505 greater than 50000 K cannot be differentiated by scale heights because there is an imperceptible

506 difference between them. What we know is that the atomic Ca is much too hot to be due to

507 impact vaporization directly. We postulate that the atomic calcium in Mercury's exosphere is the  
 508 product of Ca-bearing molecules that are ejected in the vapor cloud and subsequently dissociated  
 509 (Killen et al., 2005). Berezhnoy (2013) assigns Ca-bearing impact products as a function of  
 510 quenching temperature, along with photo-dissociation reactions, the probability of dissociation at  
 511 the Moon on a single trajectory at 3000 K, and excess energy of photolysis (see Table 4).  
 512 Photodissociation may not be the process acting at Mercury, but we give these rates as a  
 513 guideline.

514

515 Table 4. Ca-bearing molecules, dissociation pathways, probability of photodissociation on one  
 516 trajectory at 3000 K at the Moon ( $P_{\text{phot}}$ ), and excess energy of dissociation ( $E_{\text{phot}}$ ) (from  
 517 Berezhnoy, 2013).

518

Initial Product	Dissociation path	$P_{\text{phot}}$	$E_{\text{phot}}$ (eV)
Ca(OH) <sub>2</sub>	Ca(OH) <sub>2</sub> +hν=CaOH+OH	0.5	0.6
CaOH	CaOH+hν=Ca+OH	1.0	0.6
CaOH	CaOH+hν=CaO+H	0.9	0.04
CaO	CaO+hν=Ca+O	1.0	0.6

519

520

521 At Mercury, with a solar flux rate 4.6 - 10.6 times that at the Earth/Moon system, the most likely  
 522 product of impact vaporization, Ca(OH)<sub>2</sub>, (Berezhnoy, 2013), is virtually certain to dissociate to  
 523 Ca without returning to the surface. If the initial temperature of the fireball is 3500 K, the initial  
 524 energy of the products is about 0.3 eV. Either of the pathways for destruction of Ca(OH)<sub>2</sub>, the  
 525 most probable product at quenching, would result in a gain of about 1.2 eV, resulting in a neutral  
 526 Ca product with about 1.5 eV of energy. Taken at thermodynamic equilibrium, the Ca would  
 527 have a temperature of about 17500 K, consistent with the temperature derived from line widths.  
 528 In fact, given that the Ca at 1.5 eV is escaping from Mercury, and each atom subsequently  
 529 encounters lower gravity as the altitude above the surface increases, and in addition is  
 530 accelerated by radiation pressure, the apparent scale height would increase naturally with altitude  
 531 (e.g. Cassidy et al., 2014). Therefore the temperature of 70000 K derived from the Monte Carlo  
 532 code of Burger et al. (2014) may result from rapidly decreasing gravity and radiation pressure  
 533 and not from an initial 3 eV of energy. However, additional energy beyond that provided by  
 534 dissociation may be gained by recombination following ionization.

535

### 536 **5.3 Fraction of Impact-Ejected calcium in the extreme temperature regime**

537

538 The average fraction of Ca in Mercury's surface is 5.9 wt% (Evans et al., 2012). Given an  
539 average weight of all elements of 24.4, the Ca fraction by number is 3.54%. According to  
540 Berezhnoy et al. (2011) the ratio of Ca in the gas phase to Ca in all phases in the exosphere is ~  
541 0.05. Our code gives the total gas phase, including molecules. For our code, the fraction of all Ca  
542 vaporized in our models that is required to fit the measured atomic Ca varies from 2 - 12%  
543 depending on the model. Our best-fit model (Figure 7) has a fraction of vaporized Ca in the  
544 uncondensed state of 5.5%, consistent with the Berezhnoy number.

545

546 As a first order check on our model, we multiplied the total rate of gas plus melt calculated by  
547 Cintala (1992) by the fraction of Ca in the regolith, and then by 0.05 (the assumed fraction of Ca  
548 in the gas phase) to compare with the observed Ca abundance in the exosphere. Using the Ca  
549 photoionization lifetime from Huebner and Mukerjee (2011) of  $1.4 \times 10^4$  sec at Earth, (1311 s at  
550 Mercury perihelion or 3027 s at aphelion) we derived an approximate zenith column abundance  
551 of Ca of  $6.9 \times 10^8$  cm<sup>-2</sup> at perihelion, which agrees within a factor of two with the observed  
552 tangent column at dawn of about  $2 \times 10^9$  cm<sup>-2</sup> (Burger et al., 2014). Note that at the extreme  
553 temperature derived for the Ca exosphere, the ratio of the tangent column at the surface to the  
554 zenith column is only about 1.25 (See Chamberlain and Hunten, 1987, eqn. 7.1.63).

555

## 556 **6. Conclusions**

557

558 The seasonal variations in Mercury's calcium exosphere can be partially explained as being  
559 due to Mercury's radial and vertical motions through an interplanetary dust disk that is  
560 more concentrated sunwards and tipped less than 10 degrees away from Mercury's orbital  
561 plane. The best fit is tipped less than 5° from Mercury's orbital plane. Mercury's  
562 heliocentric distance varies from 0.306 AU at perihelion to 0.465 AU at aphelion, and the  
563 variations in the exospheric Ca source rate do follow the behavior that is expected from  
564 impact vaporization by interplanetary dust, with the observed seasonal variations largely  
565 due to Mercury's substantial radial excursions through the interplanetary dust-disk.  
566 However, a notable exception is a persistent enhancement seen in the calcium exosphere  
567 when Mercury's true anomaly is near  $25^\circ \pm 5^\circ$ . An enhancement in the impact vaporization  
568 rate near perihelion is attributed to excursion of Mercury through the plane of a dust disk  
569 that increases in density sunward but the peak after perihelion is more problematic.  
570 However, impact vaporization due to a single dust disk cannot explain all the variations seen in  
571 Mercury's Ca source rate; the strong peak in the Ca signal near  $\nu=25^\circ \pm 5^\circ$  requires an additional  
572 source of dust (see Fig. 1). We did consider whether the enhanced Ca signal at  $\nu=25^\circ \pm 5^\circ$  might  
573 be due to a secondary dust disk (which itself could for instance be due to a very dusty cometary

574 outburst or disintegration occurring in the recent past) that might be tilted with respect to the  
575 main dust-disk's mid-plane. Although we could obtain marginally satisfactory fits to the Ca  
576 observations using this two-disk model, the results were inconsistent with other observations of  
577 inner zodiacal light (Reach, 1991; Leinert et al., 1980; 1976; Hahn et al., 2002). If the Ca  
578 excess were in fact caused by Mercury's orbit carrying it through the midplane of such a  
579 tilted dust-disk, then a another smaller but still detectable enhancement in exospheric Ca  
580 should occur when Mercury passes through the dust-disk's midplane a second time 180  
581 degrees later in its orbit. The absence of an observed secondary enhancement in Ca at true  
582 anomaly  $25^\circ \pm 5^\circ$  degrees after aphelion limits the inclination of the primary interplanetary  
583 dust disk to less than  $10^\circ$ . The MESSENGER MASCS observations of exospheric Ca are best  
584 fit by an interplanetary dust-disk whose density varies radially as  $R^{-1.45}$  to  $R^{-2}$  (Figures 3, 4  
585 and 7) consistent with the Hahn et al. (2002) model for dust in the inner Solar System.

586  
587 We also show that the enhancement in Ca  $25^\circ \pm 5^\circ$  degrees after perihelion can be  
588 attributed to the crossing of Mercury's orbital plane and a comet stream. A likely candidate  
589 is comet 2P/Encke, even though the enhancement occurs  $\sim 25^\circ$  before Mercury crosses the  
590 comet's orbital plane. However this discrepancy is not problematic since Encke also  
591 produces several meteor showers at Earth that are spatially segregated in longitude by  
592 about  $20^\circ - 30^\circ$  around Earth's orbit (Klacka, 1999). Our model estimates that 2 - 10% of the  
593 initially vaporized calcium remains in the form of hot uncondensed Ca, bracketing the  
594 Berezhnoy (2010; 2013) estimate that globally 5% of the calcium-bearing vapor remains in the  
595 atomic uncondensed state. In our model this fraction depends on the assumed radial dependence  
596 of interplanetary dust, which governs the dust density at Mercury's orbit.

597  
598  
599 **Acknowledgments.** RMK was supported by NASA grant NNX07AR78G-S01 as a Participating  
600 Scientist on the NASA MESSENGER mission to Mercury, and by STROFIO, a NASA Mission  
601 of Opportunity on the Bepi-Colombo mission. JMH's efforts here were supported by the National  
602 Science Foundation via Grant No. AST-1313013. JMH thanks Byron Tapley for graciously  
603 providing office space and the use of the facilities at the University of Texas Center for Space  
604 Research (CSR). We thank Dr. Apostolos Christou for many helpful conversations concerning  
605 cometary dust and Dr. Matthew Burger for discussions concerning the MASCS Ca data.

606  
607 **References**  
608

609 Bereznoy, A.A., 2013. Chemistry of impact events on the Moon, *Icarus* 226, 205-211,  
610 doi:/10.1016/j.icarus.2013.05.030.

611 Bereznoy, A.A., 2010. Meteoroid bombardment as a source of the lunar exosphere. *Adv. Space*  
612 *Res.* 45, 70 - 76.

613 Bereznoy, A.A., V. Mangano, A. Mura, A. Milillo, and S. Orsini, 2011. Density distribution of  
614 metal-containing species in the exosphere of Mercury after meteoroids impacts. EPSC-DPS  
615 Joint Meeting 2011, Vol. 6, EPSC-DPS2011-1793.

616 Bereznoy, A.A. and B.A. Klumov, 2008. Impacts as sources of the exosphere on Mercury.  
617 *Icarus* 195, 511-522. doi:10.1016/j.icarus.2008.01.005.

618 Bida, T.A., R.M. Killen, and T.H. Morgan 2000. Discovery of Ca in the atmosphere of Mercury.  
619 *Nature*, 404, 159-161.

620 Borin, P., G. Cremonese, F. Marzari, M. Bruno, and S. Marchi, 2009. Statistical analysis of  
621 micrometeoroids flux on Mercury *Astron. Astrophys.* 503, 259–264. DOI: 10.1051/0004-  
622 6361/200912080.

623 Burger, M. H., R.M. Killen, W.E. McClintock, A.W. Merkel, R.J. Vervack, Jr., T.A. Cassidy,  
624 and M. Sarantos, 2014. Seasonal Variations in Mercury's Dayside Calcium Exosphere.  
625 *Icarus*, DOI: 10.1016/j.icarus.2014.04.049.

626 Burger, M. H., R.M. Killen, W.E. McClintock, R.J. Vervack, Jr., A.W. Merkel, A.L. Sprague,  
627 and M. Sarantos, 2012. Modeling MESSENGER Observations of Calcium in Mercury's  
628 Exosphere. *Journ. Geophys. Res.* 117, 0L11B, doi:10.1029/2012JE004158.

629 Burns, J. A., P.L. Lamy, and S. Soter, 1979. Radiation forces on small particles in the solar  
630 system. *Icarus* 40, 1-48, doi:10.1016/0019-1035(79)90050-2.

631 Cassidy, T.A. and R.E. Johnson, 2005. Monte Carlo model of sputtering and other ejection  
632 processes within a regolith. *Icarus* 176, 499-507, doi:10.1016/j.icarus.2005.02.013

633 Cassidy, Timothy A., Aimee W. Merkel, Matthew H. Burger, Rosemary M. Killen, William E.  
634 McClintock, Ronald J. Vervack, Jr., Menelaos Sarantos, 2014. Mercury's Seasonal Sodium  
635 Exosphere: MESSENGER Observations from Mercury Orbit, *Icarus*,  
636 10.1016/j.icarus.2014.10.037.

637 Chamberlain, J.W. and D.M. Hunten, 1987. *Theory of Planetary Atmospheres*, 2nd Ed.,  
638 Academic Press, Orlando.

639 Christou, A and D. Asher, 2009. Possible Meteoroid streams at Mercury. *Hermean Exospheres*  
640 *Workshop*, Graz, Austria, 12-13 November, 2009.

641 Cintala, M.J., 1992. Impact-Induced Thermal Effects in the Lunar and Mercurian Regoliths.  
642 *Journ. Geophys. Res.* 97, 947-973.

643 Collette, A., Z. Sternovsky, and M. Horanyi, 2014. Production of neutral gas by micrometeoroid  
644 impacts. *Icarus* 227, 89-93, doi: 10.1016/j.icarus.2013.09.009.



645 Evans, L. G., P.N. Peplowski, E.A. Rhodes, D.J. Lawrence, +10 co-authors, 2012. Major-  
646 element abundances on the surface of Mercury: Results from the MESSENGER Gamma-  
647 Ray Spectrometer, *J. Geophys. Res.*, 117, E00L07, doi:10.1029/2012JE004178.

648 Fentzke, J.T. and D. Janches, 2008. A semi-empirical model of the contribution from sporadic  
649 meteoroid sources on the meteor input function in the MLT observed at Arecibo. *Journ.*  
650 *Geophys. Res.*, 113, A03304, doi:10.1029/2007JA012531.

651 Hahn, J.M., H.A. Zook, B. Cooper, and B. Sunkara. 2002. Clementine Observations of the  
652 Zodiacal Light and the Dust Content of the Inner Solar System. *Icarus* 158, 360-378.

653 Huebner, W.F., and J. Mukherjee, Photo Rate Coefficient Database, 2011.  
654 <http://phidrates.space.swri.edu>.

655 Janches, Diego, Craig J. Heinselman, Jorge L. Chau, Amal Chandran, and Ronald Woodman,  
656 2006. Modeling the global micrometeor input function in the upper atmosphere observed by  
657 high power and large aperture radars *Journ. Geophys. Res.*, 111, A07317,  
658 doi:10.1029/2006JA011628.

659 Kameda, S., I. Yoshikawa, M. Kagitani, and S. Okano, 2009. Interplanetary dust distribution and  
660 temporal variability of Mercury's atmospheric Na. *Geophys. Res. Lett.* 36, L15201,  
661 doi:10.1029/2009GL039036.

662 Killen, R.M., T.A. Bida, and T.H. Morgan, 2005. The calcium exosphere of Mercury, *Icarus*,  
663 173#2, 300-311.

664 Klačka, Jozef. 1999. Meteor Streams of Comet Encke. Taurid Meteor Complex. [arXiv:astro-](https://arxiv.org/abs/astro-ph/9910045)  
665 [ph/9910045](https://arxiv.org/abs/astro-ph/9910045).

666 Lange, M.A. and T.J. Ahrens, 1982. The evolution of an impact generated atmosphere. *Icarus*  
667 51, 96-120.

668 Leinert, C., E. Pitz, H. Link, M. Hanner, E. Grun, H. Fechtig, J. Kissel, and P. Gammelín. 1976.  
669 Preliminary Results of the Helios A Zodiacal Light and Micrometeoroid Experiments. *Bull.*  
670 *Am. Ast. Soc.*, 8, 457.

671 Leinert, C., M. Hanner, I. Richter and E. Pitz. 1980. The Plane of Symmetry of Interplanetary  
672 Dust in the Inner Solar System. *Astron. Astrophys.* 82, 328-336.

673 Love, S.G. and D.E. Brownlee, 1993. A Direct Measurement of the Terrestrial Mass Accretion  
674 Rate of Cosmic Dust. *Science* 262, 550-553.

675 McClintock, W.E. and M.R. Lankton. 2007. The Mercury Atmospheric and Surface Composition  
676 Spectrometer for the MESSENGER Mission. *Space Science Reviews* 131, 481-521,  
677 doi:10.1007/s11214-007-9264-5.

678 Marchi, S., A. Morbidelli, and G. Cremonese, 2005. Flux of meteoroid impacts on Mercury,  
679 *Astron. Astrophys.* 431, 1123-1127. DOI: 10.1051/0004-6361:20041800 .

680 Melosh, H.J., 1989. *Impact Cratering a Geologic Process*. Oxford Univ. Press, Oxford.



681 Misconi, N.Y. and J.L. Weinberg, 1978, Is Venus concentrating interplanetary dust toward its  
682 orbital plane *Science* 200, 1484.

683 Morgan, T.H. and R.M. Killen, 1998. Production mechanisms for faint but possibly detectable  
684 coroneae about asteroids. *Planet. Space Sci.* 46, 843-850.

685 O'Keefe, J.D. and T.J. Ahrens. 1977. Impact induced energy partitioning, melting, and  
686 vaporization on terrestrial planets. *Proc. Lunar Sci. Conf.* 8th 3357-3374.

687 Reach, W.T., 1991. Zodiacal Emission II. Dust near the ecliptic. *Astrophys. Journ.* 369, 529-543.

688 Sarantos, M., Rosemary M. Killen, William E. McClintock, E. Todd Bradley, Ronald J. Vervack  
689 Jr., Mehdi Benna, James A. Slavin, Limits to Mercury's magnesium exosphere from  
690 MESSENGER second flyby observations, *Planetary and Space Science* 59 #15, 1992-2003,  
691 doi: [10.1016/j.pss.2011.05.002](https://doi.org/10.1016/j.pss.2011.05.002).

692 Selsis, F., Brillet, J., Rapaport, M., 2004. Meteor showers of cometary origin in the Solar  
693 System: Revised predictions. *Astronomy and Astrophysics*, 416, 783-789.

694 Whipple, F.L. 1940. Photographic meteor studies. III. The Taurid shower, *Proceedings of the*  
695 *American Philosophical Society* 83, 711- 745.